BCS-BEC crossover in a $(t_{2g})^4$ excitonic magnet

Nitin Kaushal,[1,2] Rahul Soni,[1,2] Alberto Nocera,[3] Gonzalo Alvarez,[4] and Elbio Dagotto[1,2]
[1]*Department of Physics and Astronomy, The University of Tennessee, Knoxville, Tennessee 37996, USA*
[2]*Materials Science and Technology Division, Oak Ridge National Laboratory, Oak Ridge, Tennessee 37831, USA*
[3]*Department of Physics and Astronomy and Stewart Blusson Quantum Matter Institute, University of British Columbia, Vancouver, B.C., Canada, V6T 1Z1*
[4]*Computational Sciences and Engineering Division and Center for Nanophase Materials Sciences, Oak Ridge National Laboratory, Oak Ridge, Tennessee 37831, USA*

(Received 18 February 2020; revised manuscript received 21 May 2020; accepted 8 June 2020; published 18 June 2020)

The condensation of spin-orbit-induced excitons in t_{2g}^4 electronic systems is attracting considerable attention. At large Hubbard U, antiferromagnetism was proposed to emerge from the Bose-Einstein Condensation (BEC) of triplons ($J_{\rm eff} = 1$). Here, we show that even at intermediate U regimes, the spin-orbit exciton condensation is possible leading also to staggered magnetic order. The canonical electron-hole excitations (excitons) transform into local triplon excitations at large U, and this BEC strong coupling regime is smoothly connected to the intermediate U excitonic insulator region. We solved the degenerate three-orbital Hubbard model with spin-orbit coupling (λ) in one dimension using the density matrix renormalization group, while in two dimensions we use the Hartree-Fock approximation (HFA). Employing these techniques, we provide the full λ versus U phase diagrams for both one- and two-dimensional lattices. Our main result is that at intermediate Hubbard U, increasing λ at fixed U the system transitions from an incommensurate spin-density-wave metal to a Bardeen-Cooper-Schrieffer (BCS) excitonic insulator, with coherence length $r_{\rm coh}$ of $\mathcal{O}(a)$ and $\mathcal{O}(10a)$ in $1d$ and $2d$, respectively, with a being the lattice spacing. Further increasing λ, the system eventually crosses over to the BEC limit (with $r_{\rm coh} \ll a$).

DOI: 10.1103/PhysRevB.101.245147

I. INTRODUCTION

The concept of excitonic condensation has attracted considerable attention since its early theoretical prediction [1]. An exciton is a bound state of an electron-hole pair. This composite particle resembles the Cooper pair of superconductors and follows hard-core bosonic statistics. Early work involving semiconductors showed that in the weak-coupling limit (small U), near the semimetal to semiconductor transition, the system can become unstable against the formation of multiple excitons [2,3]. This can lead to a condensation into a BCS-like macroscopic state called excitonic insulator. The associated BCS wavefunction can smoothly transform into a BEC state when the gap between bands increases at fixed Hubbard repulsion U. In strongly correlated systems, a BEC-like excitonic insulator can also occur in the strong coupling limit (large U). This regime attracted theoretical investigations [4–6] and was studied using large U perturbation theory, where the hopping amplitude t is the small parameter.

The extended Falicov-Kimball model has often been used as a minimal theoretical model to address excitonic condensation [7–9]. Only recently, more realistic, and more difficult, three-orbital Hubbard models were explored to study this state [10–13]. On the experimental side there have been studies showing reliable signatures of the excitonic condensate in real materials, such as in transition metal dichalcogenides [14], Ta_2NiSe_5 [15], and in bilayer systems [16,17]. To better understand excitonic insulators it is important to find additional candidate materials and additional theoretical models where this state occurs and can be studied in detail. Recently, it was recognized that materials with strong spin-orbit coupling provide a new avenue to realize this physics [18,19]. For example, Sr_2IrO_4, with Ir^{4+} ions and filling $n = 5$ electrons (t_{2g}^5), is a celebrated material due to the presence of long-range antiferromagnetic ordering in quasi-two-dimensional layers, as in superconducting cuprates [20]. Recent resonant inelastic x-ray scattering (RIXS) experiments on Sr_2IrO_4 have reported excitons as an excitation at approximately 0.5–0.6 eV [21–23]. RIXS experiments on one-dimensional stripes of Sr_2IrO_4 also indicated excitons at nearly the same energy [24]. These excitons are present in spin-orbit entangled states, hence known as *spin-orbit excitons*.

Another promising avenue for excitonic condensates induced by spin-orbit coupling involves the t_{2g}^4 case, which is the focus of the present paper. Theoretically, it was predicted that the three-orbital Hubbard model with a degenerate t_{2g} space and in the LS coupling limit ($U \gg t, \lambda$) leads to the BEC state of triplons (singlet-triplet excitations) [25–27]. We will show that these triplon excitations are low-energy manifestations of spin-orbit excitons. Dynamical Mean Field Theory (DMFT) calculations also supported similar findings [10,11], although it is difficult to distinguish between BCS and BEC states using this technique. A recent computational study of the ground state of a one-dimensional spin-orbit coupled three-orbital

Hubbard model—in a nondegenerate (tetragonal) t_{2g} space using the numerically-exact density matrix renormalization group (DMRG)—also reported a phase with staggered spin-orbit excitonic correlations [12]. All the above mentioned studies revealed an antiferromagnetic ordering accompanying the excitonic condensate. The t_{2g}^4 case is relevant for materials with Ir^{5+} ions and other $4d/5d$ transition metal oxides with the same doping $n = 4$. The presence of triplon condensation was initially discussed for double perovskite materials, such as Sr_2YIrO_6 and Ba_2YIrO_6 with a $5d^4$ configuration [28–33], but RIXS experiments showed that the triplon excitations bandwidth is not sufficiently large compared to λ to develop condensation [34]. Note that recent RIXS experiments on Ca_2RuO_4 suggests that this could be a candidate material for excitonic magnetism [35], and *ab initio* calculations have reached the same conclusion [36].

To investigate the spin-orbit excitonic condensation, in this paper, we use a simple degenerate three-orbital Hubbard model. Using numerically exact DMRG simulations on one-dimensional chains, we show that an excitonic condensation is induced accompanied by antiferromagnetic ordering even in the intermediate Hubbard regime ($U/W \approx 1$). This regime is stabilized by increasing sufficiently λ starting at the $\lambda = 0$ incommensurate spin-density wave metallic phase. These results cannot be understood using large U perturbation theories. Moreover, by using the Hartree-Fock approximation (HFA) in two-dimensional ($2d$) lattices, we also found a similar excitonic insulator phase, both in the weak and intermediate U/W regimes. As our main result, we show that there is a BCS-BEC crossover inside the excitonic condensate phase, both in $1d$ and $2d$ lattices. The BCS limit of the excitonic insulator occurs at intermediate U/W (and also for weak U/W in $2d$), and by increasing λ (at fixed U/W) the BEC state is reached. The previously known large U/W BEC state, due to triplon condensation, appears smoothly connected to the BCS excitonic insulator of intermediate U. We also provide the full λ vs U phase diagrams for $1d$ and $2d$ lattices using the many-body techniques discussed above.

The organization of this paper is as follows. In Sec. II, the model and the computational methodology used are presented. In Secs. III and IV, the main results are shown. In particular, in Sec. III, the results on $1d$ lattices using the DMRG technique are presented. In Sec. IV, the results on $2d$ lattices using HFA further support our main proposal of a BCS-BEC crossover in the model studied. In Sec. V, we discuss the overall results and present our conclusions.

II. MODEL AND METHOD

For our study, we use a degenerate three-orbital Hubbard model. The Hamiltonian has three primary terms: the tight-binding kinetic energy, the standard on-site multiorbital Hubbard interaction, and the on-site spin-orbit coupling (SOC): $H = H_K + H_{\rm int} + H_{\rm SOC}$. The tight-binding term is

$$H_K = \sum_{\langle i,j\rangle,\sigma,\gamma,\gamma'} t_{\gamma\gamma'}(c^\dagger_{i\sigma\gamma}c_{j\sigma\gamma'} + \text{H.c.}). \quad (1)$$

The hopping amplitudes $t_{\gamma\gamma'}$ connect only nearest-neighbor lattice sites (in both the $1d$ chain and $2d$ square lattices). As discussed earlier, here we use degenerate orbitals, i.e., $t_{\gamma\gamma'} = \delta_{\gamma\gamma'}t$. We fixed $t = 0.5$ and all of our results are presented in terms of dimensionless ratios, such as U/W and λ/W. The total bandwidth is $W = 4.0|t|$ and $8.0|t|$ for the $1d$ and $2d$ lattices, respectively. The orbitals used—labeled as 0, 1, and 2—could be associated respectively to the d_{yz}, d_{xz}, and d_{xy} orbitals, namely the t_{2g} sector. In real materials, the above hoppings can be much more complex [37], but nonetheless this simple model is useful to gain conceptual understanding. The on-site multiorbital Hubbard interaction term consists of the standard several components

$$H_{\rm int} = U\sum_{i,\gamma} n_{i\uparrow\gamma}n_{i\downarrow\gamma} + (U' - J_H/2)\sum_{i,\gamma<\gamma'} n_{i\gamma}n_{i\gamma'} - 2J_H\sum_{i,\gamma<\gamma'}\mathbf{S}_{i\gamma}\cdot\mathbf{S}_{i\gamma'} + J_H\sum_{i,\gamma<\gamma'}(P^\dagger_{i\gamma}P_{i\gamma'} + \text{H.c.}). \quad (2)$$

$\mathbf{S}_{i\gamma} = \frac{1}{2}\sum_{\alpha,\beta} c^\dagger_{i\alpha\gamma}\sigma_{\alpha\beta}c_{i\beta\gamma}$ represents the spin at orbital γ and lattice site i, while $n_{i\gamma}$ is the electronic density operator also at orbital γ and site i. The first two terms are the intra- and interorbital electronic repulsion, respectively. The Hund coupling is the third term, favoring the spins ferromagnetic alignment at different orbitals and the same site. Finally, the $P_{i\gamma} = c_{i\downarrow\gamma}c_{i\uparrow\gamma}$ operator in the fourth term (pair hopping) is the pair annihilation operator arising from the matrix elements of the "1/r" Coulomb repulsion as in the early studies of Kanamori. We used the standard relation $U' = U - 2J_H$ due to rotational invariance, and we fix $J_H = U/4$ for all the calculations as employed widely in previous efforts [12,13,38–40].

The SOC term is

$$H_{\rm SOC} = \lambda\sum_{i,\gamma,\gamma',\sigma,\sigma'}\langle\gamma|\mathbf{L}_i|\gamma'\rangle\cdot\langle\sigma|\mathbf{S}_i|\sigma'\rangle c^\dagger_{i\sigma\gamma}c_{i\sigma'\gamma'}, \quad (3)$$

where the coupling λ is the SOC strength.

Using the model described above, we performed calculations on one-dimensional chains employing the DMRG [41,42] for various system lengths $L = 16$, 24, and 32 sites. We kept up to 1600 states for the DMRG process and maintained a truncation error below 10^{-8} throughout the finite algorithm sweeps. We used the corrected single-site DMRG algorithm [43] with correction $a = 0.001$–0.008, and performed 35 to 40 finite sweeps to gain proper convergence depending on the system size. After this convergence, we calculated the spin-structure factor $S(q)$, orbital-structure factor $L(q)$, excitonic momentum distribution function $\Delta_{m=1/2}(q)$, and coherence length $r_{\rm coh}$. From all these observables, we constructed the phase diagram. To calculate spectral functions with the DMRG, we used the correction vector method [44], with the Krylov-space approach [45]. We obtain the single-particle spectral function $A(q,\omega)$ and the excitonic pair-pair susceptibility $\Delta_{m=1/2}(q,\omega)$. These frequency-dependent observables require considerable computational time, and multiple compute nodes. In our DMRG, we target the total $J^z_{\rm eff}$ of the system to reduce the computational cost [12]. Details of the Hartree-Fock calculations are in Ref. [46].

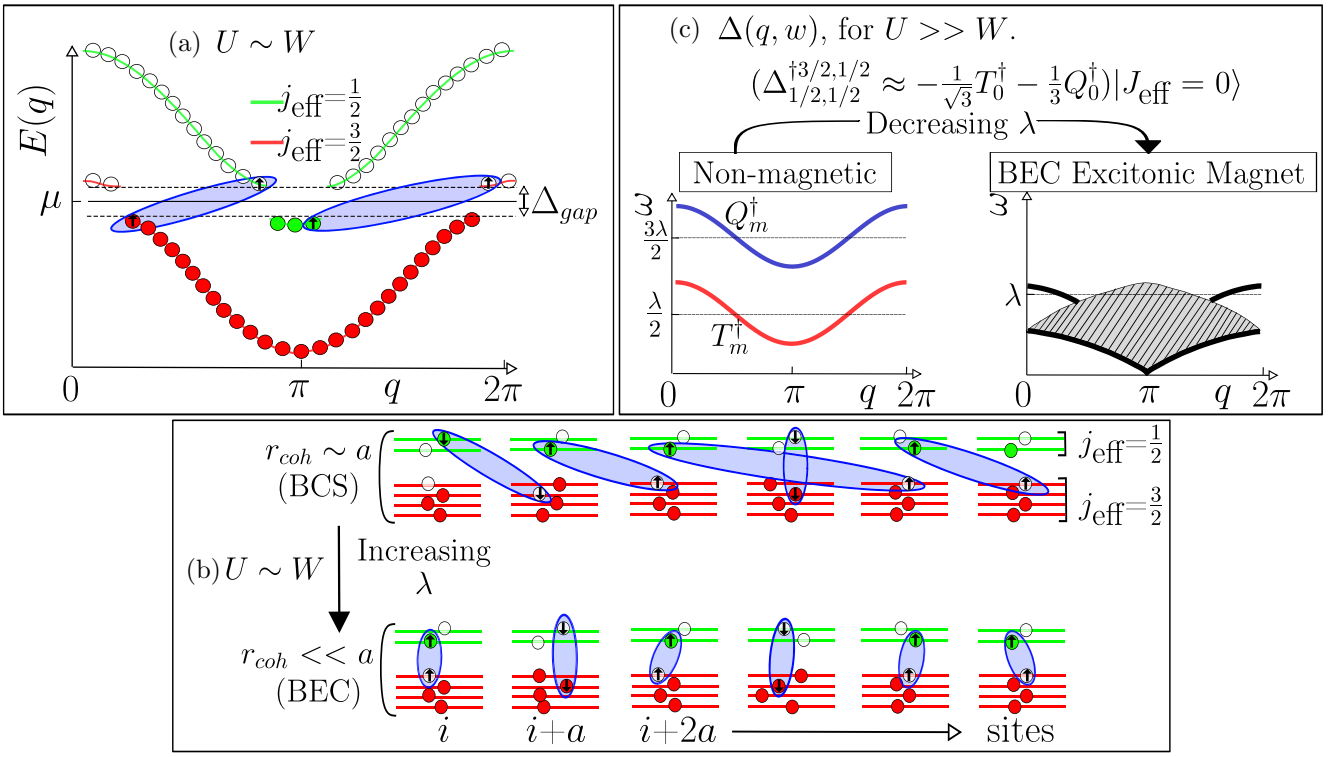

FIG. 1. Visual representation of our main results, all supported by actual DMRG and Hartree Fock calculations. In (a), the single-particle excitations of the $j_{\rm eff} = 3/2$ and $j_{\rm eff} = 1/2$ bands are shown at intermediate U, where near the chemical potential a gap opens due to the formation of excitons (note electron and hole have the same m). The $j_{\rm eff} = 3/2$ and $j_{\rm eff} = 1/2$ bands open gaps near momentum $q \approx 0$ and $q \approx \pi$, respectively. In (b), the real-space perspective of the excitonic state (at intermediate U) is shown, where the exciton's mean radius (characterized by the coherence length) decreases by increasing λ. In (c), the excitonic condensation in strong coupling is depicted. The local exciton creation operator leads to the creation of both a triplon and a quintuplon when acting on $|J_{\rm eff} = 0\rangle$. Including kinetic energy, i.e., the tight-binding term, the triplon and quintuplon excitations gain bandwidths, and decreasing λ leads to the BEC of the triplon component.

III. DMRG RESULTS IN ONE DIMENSION

Consider first the DMRG numerical results for one-dimensional chains. Figure 1 visually summarizes our conclusions. Within our numerical accuracy, we observed that the excitonic condensation starts at intermediate Hubbard $U \approx \mathcal{O}(W)$. This exciton condensation opens a gap in the $j_{\rm eff} = 3/2$ and $j_{\rm eff} = 1/2$ bands at momentum $q = 0$ and $q = \pi$, respectively, see Fig. 1(a). A similar perspective for the gap opening near the Fermi level was discussed in early research for semimetals [1]. At intermediate U, we noticed the excitons condense at finite momentum π and in the triplet channel (see Ref. [46]). We also noticed that increasing λ decreases the coherence length ($r_{\rm coh}$) of electron-hole pairs from approximately one lattice spacing (a) to a much smaller number $r_{\rm coh} \ll a$, resembling the BCS-BEC crossover. Although at extreme BCS $r_{\rm coh}$ can be as large as hundreds of lattice spacings, in our finite and one-dimensional system, we only found a robust indication for a maximum $r_{\rm coh}$ of approximately $1.0a$ which definitely is different from the atomic BEC limit. Confirming that indeed we found a BCS-BEC crossover at intermediate U, we performed mean-field calculations on $2d$ lattices (Sec. IV), where we found $r_{\rm coh}$ as large as $\mathcal{O}(10a)$ in the BCS limit.

We also found clear differences between the momentum distribution functions of the local excitations in the BCS and BEC limits in one dimension. The excitonic operator $\Delta^{\dagger 3/2,m'}_{1/2,m} = a^\dagger_{1/2,m} a_{3/2,m'}$ in the single-atom LS coupling limit can be written using triplon and quintuplon excitations (see Supplementary [46]), corresponding, respectively, to $\mathbf{T}^\dagger_n |J^z_{\rm eff} = 0, J_{\rm eff} = 0\rangle = |n, 1\rangle$, and $\mathbf{Q}^\dagger_l |J^z_{\rm eff} = 0, J_{\rm eff} = 0\rangle = |l, 2\rangle$, where $n \in \{\pm 1, 0\}$ and $l \in \{\pm 2, \pm 1, 0\}$. Calculating the pair-pair susceptibility of excitons $\Delta(q, \omega)$ for chains, in the strong-coupling nonmagnetic phase, we found bands of triplon and quintuplon excitations, with minima at $q = \pi$ but both bands are gapped. Decreasing λ drives the system to the BEC state, where $\Delta(q, \omega)$ has gapped triplon and quintuplon excitations only near $q = 0$ but mainly a continuum of excitations at other momenta above the Goldstone-like modes emerging from $q = \pi$, as sketched in Fig. 1(c).

A. Magnetic properties and staggered excitonic correlations

Now consider the results for magnetism in one-dimensional chains. We choose $U/W = 2.0$ and 10.0 as representative points for the intermediate and strong coupling regions, respectively. First, consider the intermediate coupling region where at $\lambda = 0$ we found an incommensurate spin-density wave (IC-SDW) via the spin-spin correlation $\langle \mathbf{S}_i \cdot \mathbf{S}_{i'} \rangle$ together with an exponential fast decay in the orbital-orbital correlation $\langle \mathbf{L}_i \cdot \mathbf{L}_{i'} \rangle$, as shown in Figs. 2(a,c). Block

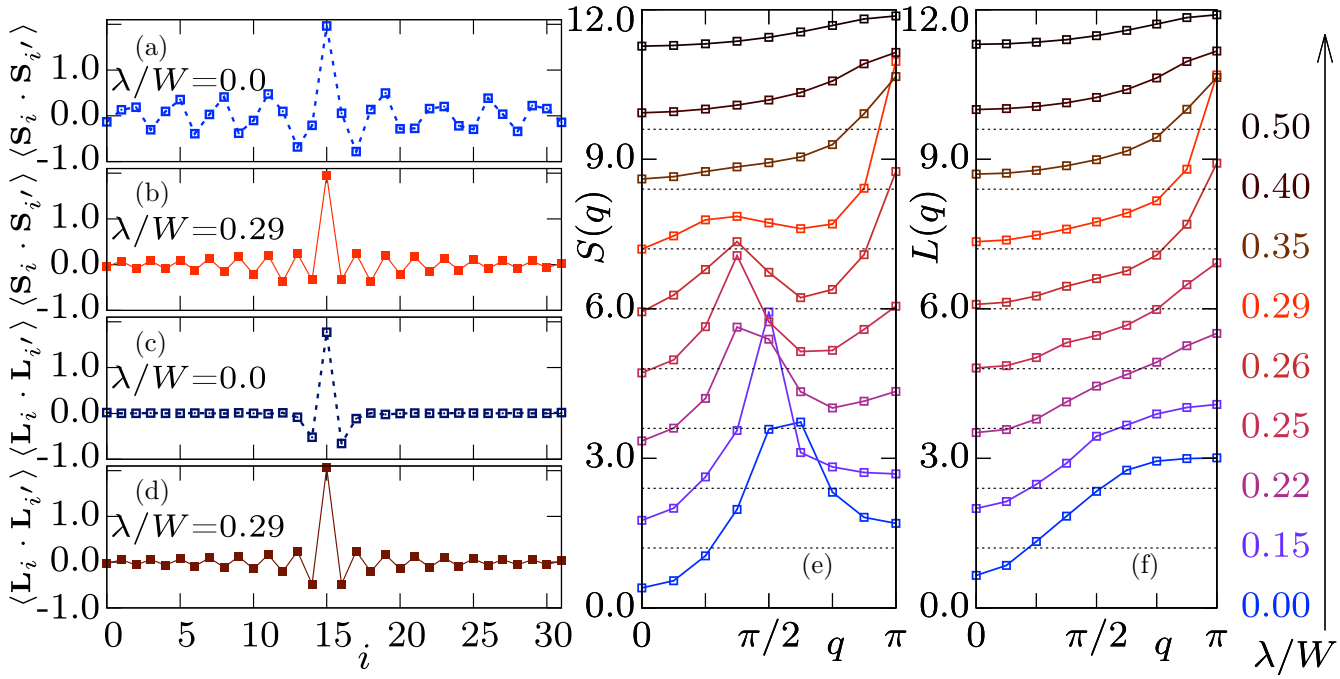

FIG. 2. DMRG results at $U/W = 2$. (a) and (b) show the real-space spin-spin correlations at $\lambda/W = 0$ and $\lambda/W = 0.29$, repectively. In (c) and (d), the real-space orbital-orbital correlations are shown at $\lambda/W = 0.0$ and $\lambda/W = 0.29$, respectively. The spin structure factor $S(q)$ and orbital structure factors $L(q)$ are in (e) and (f), respectively, for various λs. In (a)–(d), the system size was $L = 32$ and one site is fixed at the center, i.e., $i' = 15$. A system size $L = 16$ is used for (e,f).

magnetic states as in previous DMRG studies [12,38–40], do not appear in our model at $\lambda = 0$. Increasing λ drives the system towards antiferromagnetism with staggered spin-spin and orbital-orbital correlations, see Figs. 2(b) and 2(d). For additional confirmation, we show the spin structure factor $S(q) = (1/L)\sum_{j,m} e^{\imath q(j-m)}\langle \mathbf{S}_j \cdot \mathbf{S}_m\rangle$, and the orbital structure factor $L(q) = (1/L)\sum_{j,m} e^{\imath q(j-m)}\langle \mathbf{L}_j \cdot \mathbf{L}_m\rangle$ for various λ values. As λ increases, the incommensurate peak in $S(q)$ in Fig. 2(e) shifts to lower q values. The antiferromagnetic tendencies, shown by the $q = \pi$ peak, starts only near $\lambda = 0.22W$, and on further increasing λ the $q = \pi$ peak grows and the incommensurate peak is reduced. At larger λ's, the $S(q = \pi)$ peak decreases as the system transitions into the nonmagnetic state. The orbital structure factor $L(q)$ displays similar behavior at $q = \pi$. $L(q)$ starts with a flat plateaux near $q = \pi$, then grows when increasing λ, and eventually the $L(q = \pi)$ peak vanishes for very large λ, see Fig. 2(f).

In strong coupling and at $\lambda = 0$, the spins align ferromagnetically and orbital-orbital correlations show a "$+--+--$" pattern, with peaks at momentum $q = 0$ and near $q = 2\pi/3$ in $S(q)$ and $L(q)$, respectively (Fig. 3). Recent DMRG calculations on the low-energy $S = 1$ and $L = 1$ model showed similar results in the orbital correlations [47] at $\lambda = 0$. As λ increases, the system enters into the phase where orbital ordering becomes staggered, as shown by a peak at $q = \pi$ for $\lambda = 0.05W$ in Fig. 3(a). However, the spin ordering is dominantly ferromagnetic with secondary antiferromagnetic tendencies leading to a small peak at $q = \pi$ [Fig. 3(b) for $\lambda = 0.05W$]. Further increasing λ, both $L(q = \pi)$ and $S(q = \pi)$ grow while $S(q = 0)$ decreases, and ultimately $L(q = \pi)$ and $S(q = \pi)$ also start decreasing when the system enters into the nonmagnetic phase with exponentially decaying spin and orbital correlations.

In our DMRG calculations, the development of antiferromagnetic correlations in the spin and orbital channels is always accompanied by staggering in the exciton-exciton correlations, both at intermediate and strong coupling. We estimate the amount of staggering in excitonic correlation for our chains using:

$$\Delta_m = \frac{1}{L^2}\sum_{|i-i'|>0} (-1)^{|i-i'|}\left\langle \Delta^{\dagger 3/2,m}_{1/2,m}(i)\Delta^{3/2,m}_{1/2,m}(i')\right\rangle, \qquad (4)$$

where $m \in \{\pm 1/2\}$. In Fig. 3(c), the evolution of $\Delta_{1/2}$ is shown when changing λ, where each panel belongs to a different U/W. We found that smaller λ's are needed as U/W increases to obtain staggered excitonic correlations. A finite range of λ where the excitonic correlations are staggered is present for U/W as low as 1.5, although the magnitude of $\Delta_{1/2}$ decreases as U/W decreases, and for $U/W \lessapprox 1.0$, we were unable to identify—within our numerical accuracy—the region with staggered excitonic correlations. Nonetheless, it is interesting that we find staggered excitonic correlations at intermediate U, where small λ shows IC-SDW metal (for evidence of metallicity see Sec. III C). Perturbation theories at $U \gg t, \lambda$ cannot explain these results.

B. BCS-BEC crossover and IC-SDW metal to BCS-Excitonic insulator transition

Now we will discuss the main result of this paper, where we present the numerical evidence for the BCS-BEC crossover in the excitonic condensate. At intermediate U/W—the value

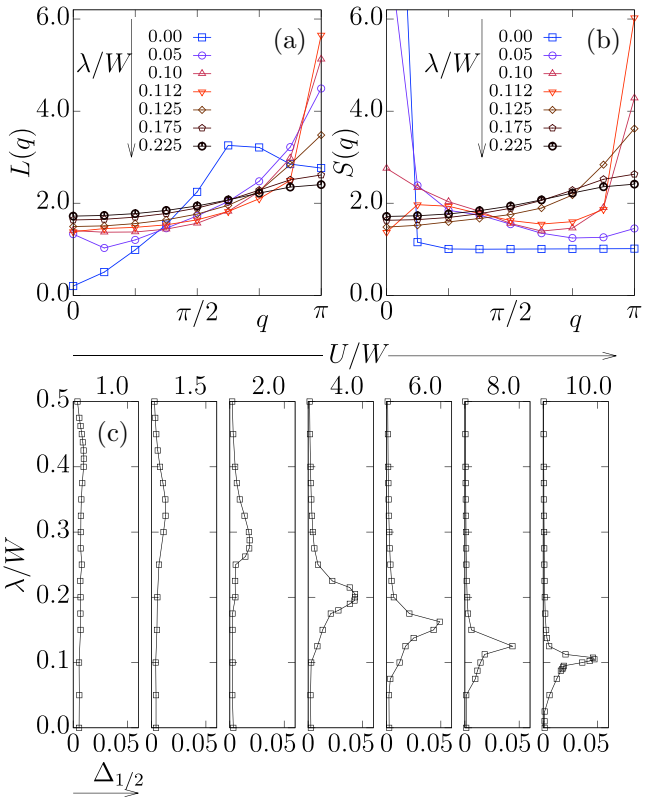

FIG. 3. Results calculated using DMRG for a one-dimensional chain of $L = 16$ sites. In (a) and (b), the orbital structure factor $L(q)$ and spin structure factor $S(q)$ are shown, respectively, at $U/W = 10$ and various λ/W's. (c) shows the measure of staggering in excitonic correlations $\Delta_{1/2}$ for various values of λ and U.

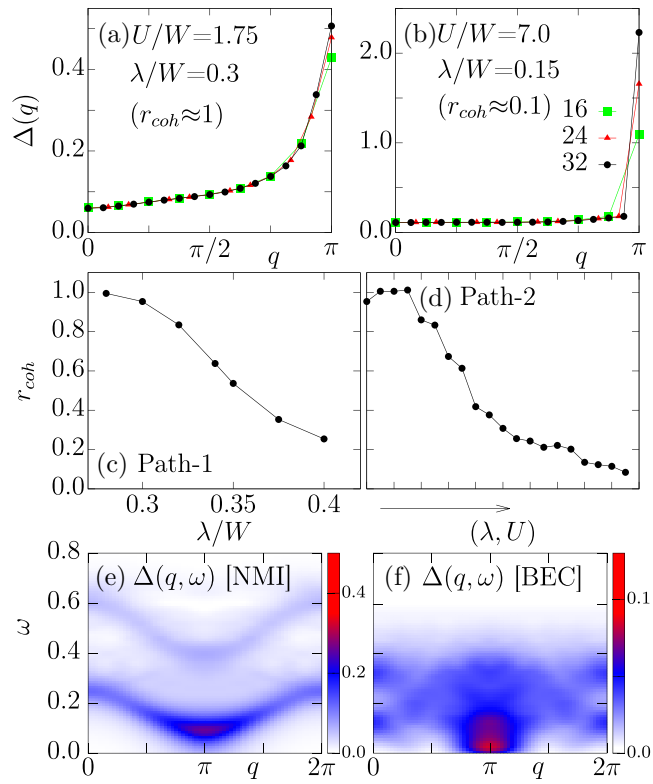

FIG. 4. (a) and (b) show the momentum distribution function of excitons $\Delta(q)$ for system sizes $L = 16,\ 24$, and 32 at two representative points of the BCS and BEC regions, respectively. (c) and (d) show the coherence length for two paths inside the excitonic condensate regime, shown in the phase diagram Fig. 6. The pair-pair susceptibilities $\Delta(q, \omega)$ are in (e) at $U/W = 10$ and $\lambda/W = 0.2$ i.e. in the nonmagnetic insulator (NMI) region, and in (f) at $U/W = 10$ and $\lambda/W = 0.11$, i.e., in the BEC region. All the calculations used DMRG.

$U/W = 1.75$ is chosen merely for simplicity—there is a finite range of $\lambda/W \in \{0.28, 0.4\}$ where staggering in excitonic, spin, and orbital correlations is present. We calculate the coherence length $r_{\rm coh}(m)$ using the widely employed formula [4,48,49]

$$r_{\rm coh}(m) = \sqrt{\frac{\sum_{ij} |i-j|^2 \langle a^\dagger_{i\frac{1}{2}\frac{m}{2}} a_{j\frac{3}{2}\frac{m}{2}} \rangle}{\sum_{ij} \langle a^\dagger_{i\frac{1}{2}\frac{m}{2}} a_{j\frac{3}{2}\frac{m}{2}} \rangle}}, \tag{5}$$

where $m \in \{\pm 1/2\}$, for the points lying inside the excitonic condensate region at fixed $U/W = 1.75$, namely, the Path-1 shown in Fig. 6. Note that $r_{\rm coh}(1/2) = r_{\rm coh}(-1/2)$. Interestingly, we found that as λ increases, $r_{\rm coh}$ decreases from nearly one lattice spacing $\approx a$ to $\approx 0.2a$, see Fig. 4(c). This reduction in the coherence length of electron-hole pairs resembles the BCS-BEC crossover already discussed in semiconductors near the semi-metal to semiconductor transition [1–3]. We also calculate $r_{\rm coh}$ for various values of λ and U when transitioning from the intermediate to the strong coupling limits, while being still inside the excitonic condensate, which we call Path-2 (see Fig. 6), as shown in Fig. 4(d). Here again we found that $r_{\rm coh}$ decreases from $\mathcal{O}(a)$ to $\mathcal{O}(0.1a)$. The ordered $(\lambda/W, U/W)$ points choosen for Path-2 are {(0.3, 1.75), (0.29,2.0), (0.29, 2.25), (0.287,2.3), (0.285,2.35), (0.283,2.4), (0.28,2.5), (0.279,2.525), (0.277,2.55), (0.275,2.6), (0.27,2.65), (0.25, 2.8), (0.24, 3.0), (0.23, 3.5), (0.21, 4.0), (0.2,4.5), (0.17, 6.0), (0.15,7.0), (0.13,9.0), (0.11, 10.0)}. Note that for $U/W \gtrapprox 2.75$, the coherence length is small as expected because at these values of U, the system is already in strong coupling for $\lambda = 0$.

In Figs. 4(a) and 4(b), we show the excitonic momentum distribution function $\Delta(q) = (1/L)\sum_{i,j}\langle e^{\imath q(i-j)} \Delta^{\dagger 3/2,m}_{1/2,m}(i) \Delta^{3/2,m}_{1/2,m}(j)\rangle$ for two points ($\lambda/W = 0.3$, $U/W = 1.75$) and ($\lambda/W = 0.15$, $U/W = 7.0$), at the intermediate U BCS and strong U BEC regions. In the BCS limit, $\Delta(q = \pi)$ grows very slightly with system size L. However, in the BEC region we found nearly linearly increasing $\Delta(q = \pi)$ with L, implying either a very slow power-law decay or even true long-range order. Such a true long-range order in our one dimension is allowed as the U(1) symmetry related to the excitonic condensation is explicitly broken by a finite Hund coupling [13]. The analysis above also clearly implies that as we increase the system size and hence increase the number of excitons, these excitons can condense also at momentum $q \neq \pi$ in the BCS limit, whereas in the BEC limit excitons condense only at $q = \pi$. For completeness, note that a similar BCS-BEC crossover has

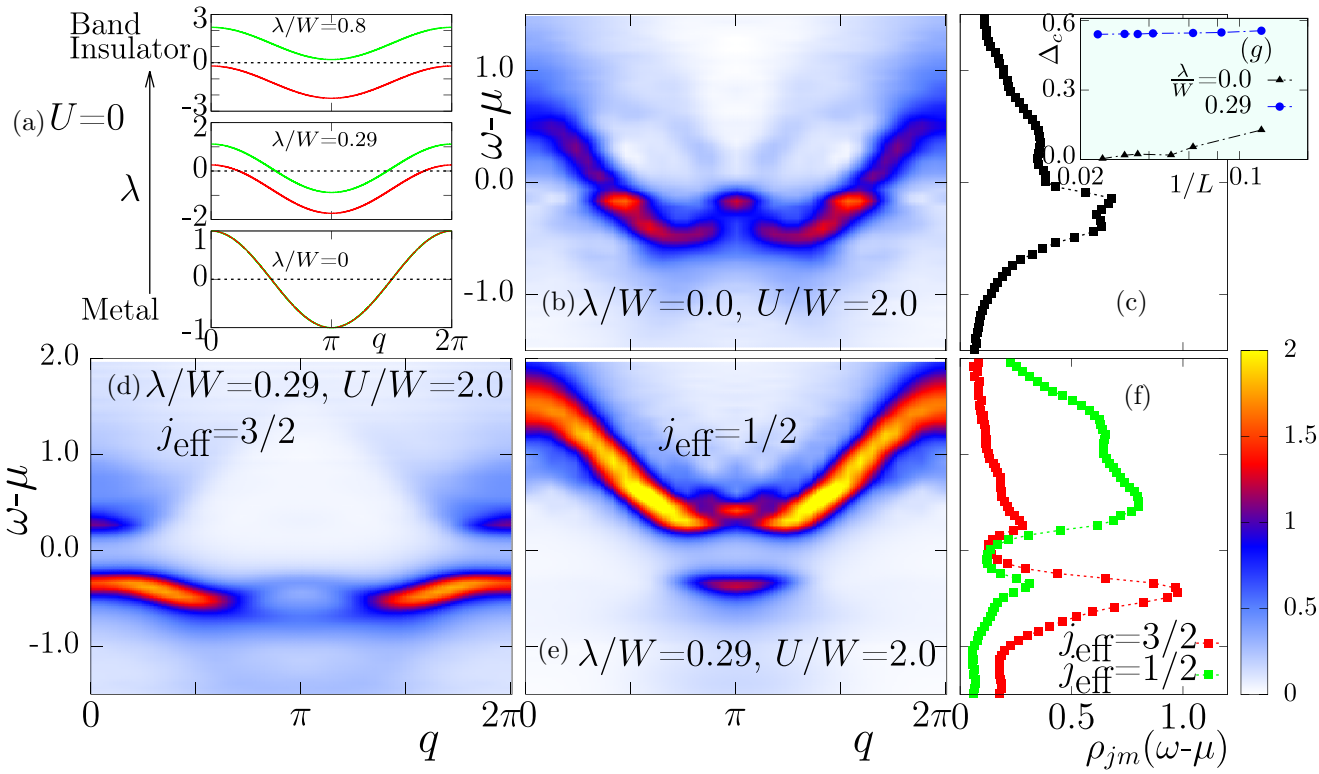

FIG. 5. The single-particle spectral function calculated using DMRG. The noninteracting band structure is shown in (a). (b) contains $A_{jm}(q,\omega)$ for $\lambda = 0$ and $U/W = 2.0$, in the IC-SDW metallic phase. In (d) and (e), $A_{jm}(q,\omega)$ at $\lambda/W = 0.29$ and $U/W = 2.0$ is shown inside the excitonic insulator phase ($r_{\rm coh} = 1.019$). (c) and (f) show the single-particle DOS [$\rho_{jm}(\omega)$] at $\lambda = 0.0$ and 0.29, respectively. The scaling of the charge gap is in inset (g) for ($U/W = 2, \lambda/W = 0$) and ($U/W = 2, \lambda/W = 0.29$).

also been reported in the extended Falicov-Kimball model in one-dimensional chains [7].

As discussed before, the exciton creation (i.e., electron-hole pair excitation) becomes the triplon and quintuplon excitation in the atomic *LS* limit. We calculated the excitonic pair-pair susceptibility

$$\Delta(q,\omega) = \langle\Psi_0|\Delta^{\dagger 3/2,1/2}_{1/2,1/2}(q)\frac{1}{\omega + i\eta - H + E_0}\Delta^{3/2,1/2}_{1/2,1/2}(q)|\Psi_0\rangle \tag{6}$$

at large $U/W = 10.0$ on one-dimensional chains to study the effect of the kinetic energy. The broadening η was 0.05eV. We choose two values $\lambda/W = 0.20$ and $\lambda/W = 0.11$ in the nonmagnetic insulator and BEC regions, respectively [Figs. 4(e) and 4(f)]. For the nonmagnetic state, we found the pair-pair susceptibility shows two cosine-like bands with minima at $q = \pi$, where the lower band belongs to $\Delta J_{\rm eff} = 1$ (triplon) and the upper band represent $\Delta J_{\rm eff} = 2$ excitations, as in previous analytical studies [27]. The BEC is expected to occur by reducing λ, when the lower band of triplons becomes gapless. In our BEC state, $\Delta(q,\omega)$ shows features very different from those in the nonmagnetic state: after removing the elastic peak we found that two gapped bands appear only near $q = 0$, and the spectrum at $q = \pi$ is now gapless with emerging Goldstone-like modes. We also found continuum-like features for $q \in \{-\frac{\pi}{4}, \frac{7\pi}{4}\}$.

In the noninteracting limit, λ only splits the $j_{\rm eff} = 3/2$ and $j_{\rm eff} = 1/2$ bands, see Fig. 5(a), driving a metal to band-insulator transition. Only at finite U the excitonic condensation happens: as shown in our DMRG results, $U/W \gtrapprox 1.0$ is required to obtain a noticeable staggering in the excitonic correlations. To further investigate the intermediate U region, we calculated the single-particle spectral function $A_{jm}(q,\omega)$ (see Ref. [46]) at $U/W = 2$, using both $\lambda = 0.0$ and $\lambda/W = 0.29$ corresponding to the IC-SDW and excitonic condensate with $r_{\rm coh} \approx 1.0$ (BCS limit), respectively. In Fig. 5(b), we show $A_{jm}(q,\omega-\mu)$ for $\lambda = 0$: at this point all $(j_{\rm eff}, m)$ states are degenerate. Comparing to the noninteracting limit band structure, a renormalization of the bands is clearly visible, having two minima structure and a local maxima at $q = \pi$, as a consequence of the Hubbard repulsion. In this phase, the nesting vector at the chemical potential μ decides the ordering vector of the incommensurate spin-density wave. We also show the single-particle density of states $\rho_{jm}(\omega-\mu)$, Fig. 5(c), which indicates that the system has a finite density of states at μ suggesting this phase is metallic.

Figures 5(d) and 5(e) show $A_{j,m}(q,\omega-\mu)$ for $j_{\rm eff} = 3/2$ (all $m \in \{\pm 3/2, \pm 1/2\}$ are degenerate) and $j_{\rm eff} = 1/2$ (both $m \in \{\pm 1/2\}$ are degenerate), respectively. The gaps at μ, at wavevectors $q \approx 0$ and $q \approx \pi$ in the spectral functions of $j_{\rm eff} = 3/2$ and $j_{\rm eff} = 1/2$, respectively, are clearly present. These gaps appear due to the formation of bound states of electrons and holes, arising from the $q \approx 0$ and $q \approx \pi$ states of the $j_{\rm eff} = 3/2$ and $j_{\rm eff} = 1/2$ bands, respectively. This leads to excitons creation with net momentum $\approx \pi$ (indirect excitons). We also noticed a nontrivial suppression of the

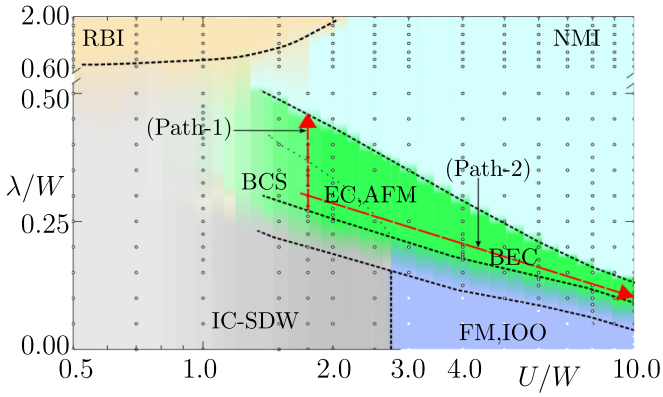

FIG. 6. λ/W vs U/W phase diagram calculated using DMRG for a one-dimensional system. The two red arrows corresponds to the paths used in (c) and (d) of Fig. 4. The vertical red arrow is chosen at $U/W = 1.75$, and depicts Path-1 of Fig. 4(c). The diagonal red arrow corresponds to the Path-2 used in Fig. 4(d). The notation RBI, IC-SDW, FM, IOO, EC, AFM, and NMI stands for relativistic band insulator, incommensurate spin-density wave, ferromagnetic, excitonic condensate, antiferromagnetic, and nonmagnetic insulator, respectively.

spectral function near $q = \pi$ for $j_{\text{eff}} = 3/2$, below μ, but the explanation for these small features requires further work. However, it is evident that the gap opens due to the formation of indirect excitons and eventually leads to a BCS-like state. In Fig. 5(f), the j-resolved density-of-states is shown to illustrate the suppression near μ for both the $j_{\text{eff}} = 3/2$ and $1/2$ bands. A small but finite density-of-states at μ is present because of the broadening η used. To confirm the transition from metal (at $\lambda = 0$) to excitonic insulator (at $\lambda/W = 0.29$), we performed finite-size scaling of the charge gap $\Delta_c = E_G(N+1) + E_G(N-1) - 2E_G(N)$ for both points, see Fig. 5(g). At $\lambda = 0.29$, using system sizes $L = 8,\ 12,\ 16,\ 24,\ 32$, and 42, we found the charge gap is quite robust 0.55 eV. Sizes $L = 8,\ 16,\ 20,\ 28,\ 32$, and 40 were used for the scaling at $\lambda = 0$, which indicates that Δ_c scales to $\approx$0 eV in the thermodynamic limit.

Figure 6 ends this section by displaying the full λ vs U phase diagram for our one-dimensional systems. The CPU-costly DMRG calculations were performed for all small circles shown using a system size $L = 16$. After obtaining the ground state, then spin-spin correlations, orbital-orbital correlations, and exciton-exciton correlations were calculated to analyze the properties of each phase. The (j_{eff}, m)-resolved local electronic densities were also studied to identify the relativistic band insulator phase. The dashed line inside the excitonic condensate region (green region) is a guide to the eyes to show the BCS and BEC limits of the excitonic condensate.

IV. HARTREE-FOCK RESULTS IN TWO-DIMENSIONS

In this section, we will present and discuss the results obtained in two-dimensional lattices by performing mean-field calculations in real-space. Hartree-Fock approximations are appropriate to study excitonic condensates as shown in the original publications that started this field [1], as well as in recent numerical calculations on Falicov-Kimball models [8,50].

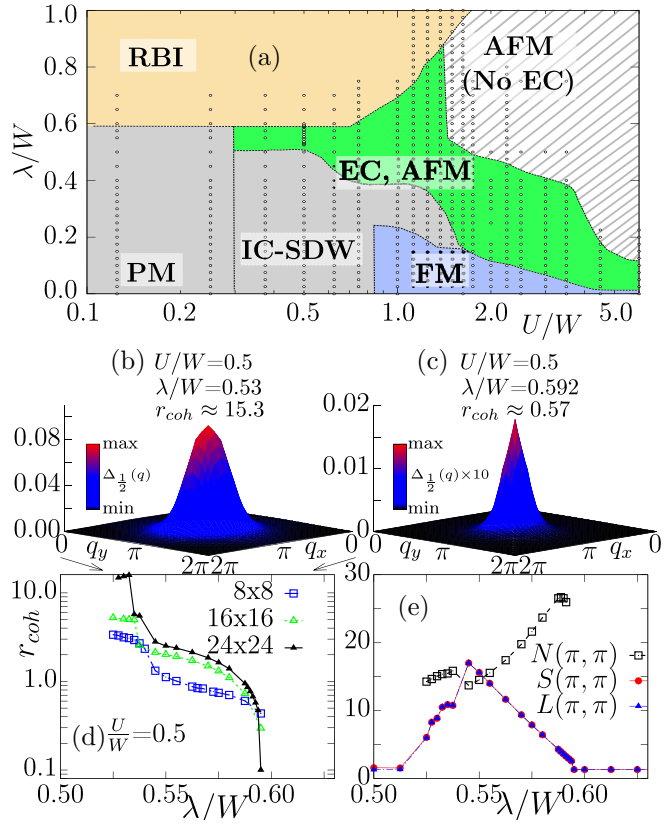

FIG. 7. (a) shows the λ vs U phase diagram for the square lattice, calculated using the Hartree-Fock approximation. In (b) and (c), the momentum distribution function of excitons $\Delta(\mathbf{q})$ is shown at $\lambda = 0.53$ and $\lambda/W = 0.592$, respectively, for fixed $U/W = 0.5$ and a 24×24 system. The coherence length for various values of λ, at fixed $U/W = 0.5$, for system sizes 8×8, 16×16, and 24×24 are in (d). The $N(\pi,\pi)$, $S(\pi,\pi)$, and $L(\pi,\pi)$ are in (e) for various values of λ, at fixed $U/W = 0.5$ and using a 24×24 cluster.

In Fig. 7(a), we show the full λ versus U phase diagram for the two-dimensional lattice. To identify the various phases, we calculated the spin structure factor and orbital structure factor on 16×16 clusters with periodic boundary conditions for all the points explicitly shown in the phase diagram. Our mean-field calculations in two dimensions capture almost all the phases found in our numerical exact one-dimensional results, the main difference being having shifted boundaries, to be expected considering the different dimensionality and different many-body approximations. The only important difference is that our mean-field calculations do not capture the nonmagnetic phase in strong coupling, because the lattice nonmagnetic state can be written as a direct product of $J_{\text{eff}} = 0$ at each site, i.e., $|J_{\text{eff}=0}\rangle_i \otimes |J_{\text{eff}=0}\rangle_{i+1} \otimes |J_{\text{eff}=0}\rangle_{i+2} \ldots$, where each $J_{\text{eff}} = 0$ state in the LS coupling limit is a sum of Slater determinants. However, the excitonic condensate phase, the focus of the present paper, is properly captured by Hartree-Fock and it is present even in a larger region of the phase diagram than in one dimension, hence giving us a good opportunity to discuss the BCS-BEC crossover in two-dimensional lattices. We confirmed that increasing λ the system transits from IC-SDW

metal to excitonic insulator at intermediate U, by calculating single particle density-of-states (see Ref. [46]). It must be noted that excitonic magnet, at large U, found in Hartree-Fock calculations cannot be described by condensation of triplons. In the intermediate U region, the band insulator is present at large λ with excitons as local objects and the band gap is larger than the binding energy of excitons. As λ decreases, the excitonic magnet emerges due to the condensation of these conventional excitons. The above described scenario can be captured in mean-field theory calculations leading to the exctionic condensate state, as discussed earlier [1].

To proceed with our discussion, we fix $U/W = 0.5$ ($W = 8t$) where the excitonic condensation is present in a narrow but finite range of spin-orbit coupling, while for smaller λ's the IC-SDW phase is present. Similar to our one-dimensional DMRG calculations, in two dimensions we found that inside the excitonic condensate region (at a fixed weak or intermediate U/W values), $r_{\rm coh}$ decreases on increasing λ, as shown in Fig. 7(d) depicting the BCS-BEC crossover. We have calculated $r_{\rm coh}$ for system sizes 8×8, 16×16, and 24×24. We found that in the BCS limit, $r_{\rm coh}$ increases as the system size increases and $r_{\rm coh}$ can reach values as high as $\approx 15.0a$ for the 24×24 lattice. This clearly supports our claim for the presence of the BCS state above the IC-SDW region, as in our DMRG chain calculations.

On the other hand, in the BEC limit, below the relativistic band insulator in the phase diagram, $r_{\rm coh}$ is $\mathcal{O}(0.1a)$, as shown in Fig. 7(d). Figure 7(e) displays $S(\pi,\pi)$ and $L(\pi,\pi)$, for $U/W = 0.5$, showing that only for a finite range of λ the antiferromagnetic ordering develops. We also show the momentum distribution function of excitons $\Delta_{1/2}(\mathbf{q})$ at $\lambda/W = 0.53$ and $\lambda/W = 0.592$ in the BCS and BEC limits, respectively. In the BEC limit, $\Delta(\mathbf{q})$ is much sharper near $\mathbf{q} = (\pi,\pi)$ than in the BCS limit, as expected because in BEC a larger ratio of excitons is expected at the condensation momentum than other momenta. To further investigate the above claim we calculated the ratio of excitons at wave vector $\mathbf{q} = (\pi,\pi)$ and at other wave vectors using $N(\pi,\pi) = \Delta_{1/2}(\pi,\pi)/\langle\Delta_{1/2}(\mathbf{q} \neq (\pi,\pi))\rangle$, where $\langle\Delta_{1/2}(\mathbf{q} \neq (\pi,\pi))\rangle = \frac{1}{L^2-1}\sum_{\mathbf{q}\neq(\pi,\pi)} \Delta_{1/2}(\mathbf{q})$. It is evident from Fig. 7(e) that $N(\pi,\pi)$ increases as we transition from the BCS to the BEC limits.

V. CONCLUSIONS

In this publication, we studied the degenerate $(t_{2g})^4$ multiorbital Hubbard model in the presence of spin-orbit coupling, using one-dimensional chains and numerically exact DMRG and also using two-dimensional clusters within the Hartree-Fock approximation. In both calculations, we provide evidence for a BCS-BEC crossover in the spin-orbit excitonic condensate, in the regime of robust Hund coupling fixed as $J_H = U/4$. Within our accuracy, we established that in this model and at intermediate U/W, the system transits from an IC-SDW metallic phase to the BCS limit of an antiferromagnetic excitonic condensate. Further increasing λ the coherence length of electron-hole pairs decreases rapidly as the system crossovers to the BEC regime. This BEC regime ends as eventually the system transits to the relativistic band insulator on increasing further λ. Our work provides the first indications of a BCS-BEC crossover in the excitonic magnetic state at intermediate U/W, a region of couplings that cannot be explored within approximations developed in the large U/W regime.

We hope our results encourage further theoretical and experimental investigations on t_{2g}^4 compounds with robust spin-orbit coupling. Although our study is performed using degenerate orbitals, we believe that our findings could be generic and relevant for materials showing magnetic excitonic condensation at intermediate values of the Hubbard repulsion and spin-orbit coupling.

ACKNOWLEDGMENTS

N.K., R.S., and E.D. were supported by the U.S. Department of Energy (DOE), Office of Science, Basic Energy Sciences (BES), Materials Sciences and Engineering Division. A.N. was supported by the Canada First Research Excellence Fund. G.A. was supported by the Scientific Discovery through Advanced Computing (SciDAC) program funded by the U.S. DOE, Office of Science, Advanced Scientific Computing Research and Basic Energy Sciences, Division of Materials Sciences and Engineering. Part of this work was conducted at the Center for Nanophase Materials Sciences, sponsored by the Scientific User Facilities Division (SUFD), BES, DOE, under contract with UT-Battelle.

[1] D. Jérome, T. M. Rice, and W. Kohn, Phys. Rev. **158**, 462 (1967); B. I. Halperin and T. M. Rice, Rev. Mod. Phys. **40**, 755 (1968); Solid State Phys. **21**, 115 (1968).
[2] N. F. Mott, Philos. Mag. **6**, 287 (1961).
[3] R. S. Knox, in *Solid State Physics* (Academic Press Inc., New York, 1963), Suppl. 5, p. 100.
[4] J. Kunes, J. Phys.: Condens. Matter **27**, 333201 (2015).
[5] C. D. Batista, J. E. Gubernatis, J. Bonca, and H. Q. Lin, Phys. Rev. Lett. **92**, 187601 (2004).
[6] K. Sugimoto, S. Nishimoto, T. Kaneko, and Y. Ohta, Phys. Rev. Lett. **120**, 247602 (2018).
[7] S. Ejima, T. Kaneko, Y. Ohta, and H. Fehske, Phys. Rev. Lett. **112**, 026401 (2014).
[8] K. Seki, R. Eder, and Y. Ohta, Phys. Rev. B **84**, 245106 (2011).
[9] V. N. Phan, K. W. Becker, and H. Fehske, Phys. Rev. B **81**, 205117 (2010).
[10] T. Sato, T. Shirakawa, and S. Yunoki, Phys. Rev. B **99**, 075117 (2019).
[11] A. J. Kim, H. O. Jeschke, P. Werner, and R. Valentí, Phys. Rev. Lett. **118**, 086401 (2017).
[12] N. Kaushal, J. Herbrych, A. Nocera, G. Alvarez, A. Moreo, F. A. Reboredo, and E. Dagotto, Phys. Rev. B **96**, 155111 (2017).
[13] N. Kaushal, A. Nocera, G. Alvarez, A. Moreo, and E. Dagotto, Phys. Rev. B **99**, 155115 (2019).
[14] A. Kogar, M. S. Rak, S. Vig, A. A. Husain, F. Flicker, Y. Il Joe, L. Venema, G. J. MacDougall, T. C. Chiang, E. Fradkin, J. van Wezel, and P. Abbamonte, Science **358**, 1314 (2017).

[15] Y. F. Lu, H. Kono, T. I. Larkin, A. W. Rost, T. Takayama, A. V. Boris, B. Keimer, and H. Takagi, Nat. Commun. **8**, 14408 (2017).

[16] J. P. Eisenstein and A. H. MacDonald, Nature (London) **432**, 691 (2004).

[17] G. William Burg, N. Prasad, K. Kim, T. Taniguchi, K. Watanabe, A. H. MacDonald, L. F. Register, and E. Tutuc, Phys. Rev. Lett. **120**, 177702 (2018).

[18] G. Cao and P. Schlottman, Rep. Prog. Phys. **81**, 042502 (2018).

[19] J. G. Rau, E. K.-H. Lee, and H.-Y. Kee, Annu. Rev. Condens. Matter Phys. **7**, 195 (2016).

[20] B. J. Kim, H. Jin, S. J. Moon, J.-Y. Kim, B.-G. Park, C. S. Leem, J. Yu, T. W. Noh, C. Kim, S.-J. Oh, J.-H. Park, V. Durairaj, G. Cao, and E. Rotenberg, Phys. Rev. Lett. **101**, 076402 (2008).

[21] M. Souri, B. H. Kim, J. H. Gruenewald, J. G. Connell, J. Thompson, J. Nichols, J. Terzic, B. I. Min, G. Cao, J. W. Brill, and A. Seo, Phys. Rev. B **95**, 235125 (2017).

[22] J. Kim, D. Casa, M. H. Upton, T. Gog, Y.-J. Kim, J. F. Mitchell, M. van Veenendaal, M. Daghofer, J. van den Brink, G. Khaliullin, and B. J. Kim, Phys. Rev. Lett. **108**, 177003 (2012).

[23] J. Kim, M. Daghofer, A. H. Said, T. Gog, J. van den Brink, G. Khaliullin, and B. J. Kim, Nat. Commun. **5**, 4453 (2014).

[24] J. H. Gruenewald, J. Kim, H. S. Kim, J. M. Johnson, J. Hwang, M. Souri, J. Terzic, S. H. Chang, A. Said, J. W. Brill, G. Cao, H. Y. Kee, and S. S. A. Seo, Adv. Mater. **29**, 1603798 (2016)

[25] G. Khaliullin, Phys. Rev. Lett. **111**, 197201 (2013).

[26] O. N. Meetei, W. S. Cole, M. Randeria, and N. Trivedi, Phys. Rev. B **91**, 054412 (2015).

[27] C. Svoboda, M. Randeria, and N. Trivedi, Phys. Rev. B **95**, 014409 (2017).

[28] G. Cao, T. F. Qi, L. Li, J. Terzic, S. J. Yuan, L. E. DeLong, G. Murthy, and R. K. Kaul, Phys. Rev. Lett. **112**, 056402 (2014).

[29] T. Dey, A. Maljuk, D. V. Efremov, O. Kataeva, S. Gass, C. G. F. Blum, F. Steckel, D. Gruner, T. Ritschel, A. U. B. Wolter, J. Geck, C. Hess, K. Koepernik, J. van den Brink, S. Wurmehl, and B. Büchner, Phys. Rev. B **93**, 014434 (2016).

[30] L. T. Corredor, G. Aslan-Cansever, M. Sturza, Kaustuv Manna, A. Maljuk, S. Gass, T. Dey, A. U. B. Wolter, Olga Kataeva, A. Zimmermann, M. Geyer, C. G. F. Blum, S. Wurmehl, and B. Büchner, Phys. Rev. B **95**, 064418 (2017).

[31] J. Terzic, H. Zheng, Feng Ye, H. D. Zhao, P. Schlottmann, L. E. De Long, S. J. Yuan, and G. Cao, Phys. Rev. B **96**, 064436 (2017).

[32] S. Fuchs, T. Dey, G. Aslan-Cansever, A. Maljuk, S. Wurmehl, B. Büchner, and V. Kataev, Phys. Rev. Lett. **120**, 237204 (2018).

[33] A. Nag, S. Bhowal, A. Chakraborty, M. M. Sala, A. Efimenko, F. Bert, P. K. Biswas, A. D. Hillier, M. Itoh, S. D. Kaushik, V. Siruguri, C. Meneghini, I. Dasgupta, and S. Ray, Phys. Rev. B **98**, 014431 (2018).

[34] M. Kusch, V. M. Katukuri, N. A. Bogdanov, B. Buchner, T. Dey, D.V. Efremov, J. E. Hamann-Borrero, B. H. Kim, M. Krisch, A. Maljuk, M. M. Sala, S. Wurmehl, G. Aslan-Cansever, M. Sturza, L. Hozoi, J. van den Brink, and J. Geck, Phys. Rev. B **97**, 064421 (2018).

[35] H. Gretarsson, H. Suzuki, Hoon Kim, K. Ueda, M. Krautloher, B. J. Kim, H. Yavaş, G. Khaliullin, and B. Keimer, Phys. Rev. B **100**, 045123 (2019).

[36] T. Feldmaier, P. Strobel, M. Schmid, P. Hansmann, and M. Daghofer, arXiv:1910.13977.

[37] M. Daghofer, A. Nicholson, and A. Moreo, and E. Dagotto, Phys. Rev. B **81**, 014511 (2010).

[38] J. Herbrych, J. Heverhagen, N. D. Patel, G. Alvarez, M. Daghofer, A. Moreo, and E. Dagotto, Phys. Rev. Lett. **123**, 027203 (2019).

[39] N. D. Patel, A. Nocera, G. Alvarez, A. Moreo, S. Johnston, and E. Dagotto, Commun. Phys. **2**, 64 (2019).

[40] J. Herbrych, N. Kaushal, A. Nocera, G. Alvarez, A. Moreo, and E. Dagotto, Nat. Commun. **9**, 3736 (2018).

[41] S. R. White, Phys. Rev. Lett. **69**, 2863 (1992).

[42] S. R. White, Phys. Rev. B **48**, 10345 (1993).

[43] S. R. White, Phys. Rev. B **72**, 180403(R) (2005).

[44] T. D. Kühner and S. R. White, Phys. Rev. B **60**, 335 (1999).

[45] A. Nocera and G. Alvarez, Phys. Rev. E **94**, 053308 (2016).

[46] See Supplemental Material at http://link.aps.org/supplemental/10.1103/PhysRevB.101.245147 for the atomic limit, representation of spin orbit exciton operators in the *LS* coupling limit, condensation of excitons in the triplet channel, details of the DMRG spectral function calculations, and details of the Hartree-Fock calculations.

[47] S. Feng, N. D. Patel, P. Kim, J. H. Han, and N. Trivedi, Phys. Rev. B **101**, 155112 (2020).

[48] T. Kaneko, S. Ejima, H. Fehske, and Y. Ohta, Phys. Rev. B **88**, 035312 (2013).

[49] T. Kaneko and Y. Ohta, Phys. Rev. B **90**, 245144 (2014).

[50] P. Farkašovský, Phys. Rev. B **95**, 045101 (2017).